

Experimental and theoretical study of the effect of gas flow on gas temperature in an atmospheric pressure microplasma

Qiang Wang¹, Florian Doll², Vincent M Donnelly¹,
Demetre J Economou¹, Nader Sadeghi³ and Gerhard F Franz²

¹ Plasma Processing Laboratory, Department of Chemical and Biomolecular Engineering, University of Houston, Houston, TX 77204-4004, USA

² University of Applied Sciences, Munich, Bavaria, Germany

³ Laboratoire de Spectrométrie Physique, Université J Fourier de Grenoble & CNRS, BP 87, F-38402 Saint-Martin d'Hères Cedex, France

E-mail: vmdonnelly@uh.edu and economou@uh.edu

Received 29 March 2007, in final form 21 May 2007

Published 29 June 2007

Online at stacks.iop.org/JPhysD/40/4202

Abstract

The dependence of gas temperature on gas flow through a direct current, slot-type, atmospheric pressure microplasma in helium or argon was investigated by a combination of experiments and modelling. Spatially resolved gas temperature profiles across the gap between the two electrodes were obtained from rotational analysis of $N_2(C^3\Pi_u \rightarrow B^3\Pi_g)$ emission spectra, with small amounts of N_2 added as actinometer gas. In Ar/ N_2 discharges, the $N_2(C^3\Pi_u v' = 0 \rightarrow B^3\Pi_g v'' = 0)$ emission spectra were fitted with a two-temperature population distribution of the $N_2(C)$ state, and the gas temperature was obtained from the 'low temperature' component of the distribution. Under the same input power of 20 kW cm^{-3} , the peak gas temperature in helium ($\sim 650 \text{ K}$) was significantly lower than that in argon (over 1200 K). This reflects the much higher thermal conductivity of helium gas. The gas temperature decreased with increasing gas flow rate, more so in argon compared with helium. This was consistent with the fact that conductive heat losses dominate in helium microplasmas, while convective heat losses play a major role in argon microplasmas. A plasma-gas flow simulation of the microdischarge, including a chemistry set, a compressible Navier–Stokes (and mass continuity) equation and a convective heat transport equation, was also performed. Experimental measurements were in good agreement with simulation predictions.

1. Introduction

High pressure (100s of Torr) microplasmas (also called microdischarges) have been the subject of much research. These studies are motivated by numerous potential applications of microdischarges, including ultraviolet and vacuum ultraviolet light sources, sensors, microelectromechanical systems and microreactors [1–5]. Many of the proposed configurations of microplasma sources involve gas flow in microchannels combined with heat transport and chemical reactions. For example, a RF microplasma jet was used for

thin film processing [4], a slot-type microplasma with gas flow could serve as a UV optical emission source [6], and a microhollow cathode was tested as a flow microreactor [5].

Understanding the combined momentum, heat and mass transport, coupled with chemical reactions in the microplasma channel, is very important for maintaining stable discharges as well as for optimizing the functionality of such microdevices. A number of studies have been reported for microreactors without a plasma. Investigations of convective gas flow through microchannels [7] indicate that there are significant differences in gas dynamics in a microchannel compared

with conventional large size reactors. For example, gas flow in a microreactor may be rarefied, with velocity slip and temperature jumps on the walls [8]; or the Nusselt number for heat transfer (a dimensionless heat transfer coefficient) can be higher than that predicted for fully developed flow in conventional channels [9]; or the gas dynamics may critically depend on the roughness of the surface, because of the large surface-to-volume ratio in microchannels [10].

Adding a plasma can further complicate the gas transport and reaction chain in microplasma systems, especially at atmospheric pressure. In particular, due to power deposition of tens of kW cm^{-3} , plasma induced gas heating can be significant [11, 12], having a profound influence on gas dynamics and chemistry. In addition, momentum transfer from ions to the neutral gas may cause local flow patterns in the microchannel, even in the absence of external flow [11]. On the other hand, gas dynamics affects plasma parameters such as neutral, electron and ion species density, as well as electron temperature [13, 14].

In this work, a direct current, atmospheric pressure, slot-type microplasma in helium or argon was studied, with particular emphasis on the effect of convective gas flow on the gas temperature and its distribution in the microplasma channel. Spatially resolved measurements of gas temperature between the parallel-plate electrodes as a function of gas flow rate were obtained. Experimental results were compared with the predictions of a plasma-gas dynamics model used for fundamental understanding of the microplasma source.

2. Experimental

The experimental setup is sketched in figure 1. The slot-type microplasma source consisted of a $200 \mu\text{m}$ wide, 8 mm long slot cut through a three-layer structure with a metal ($500 \mu\text{m}$

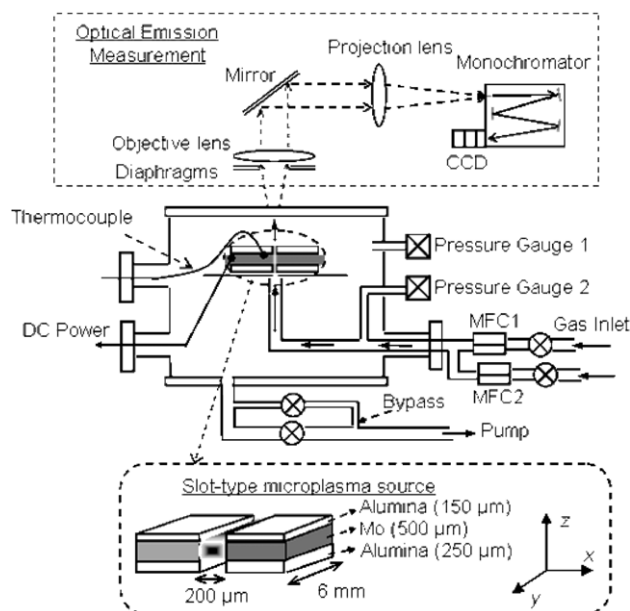


Figure 1. Schematic of the experimental setup to study the effect of gas flow through a microplasma channel. Also shown are the slot-type microplasma source configuration (bottom) and the setup for OES measurements (top).

thick Mo) sandwiched between two (250 and $150 \mu\text{m}$ thick Al_2O_3) dielectric layers. (Actually, each Mo electrode was 6 mm long; there was a 1 mm dielectric clearance on either end of the slot.) The microplasma source was installed in a vacuum chamber to maintain a pure gas environment. In this flow configuration, He or Ar with trace amounts of N_2 was introduced at the bottom of the sample holder, so that all gas would flow through the slot of the microplasma source. Gas flow rate (0 – 2000 sccm) was controlled by mass flow controllers, and both the upstream and downstream pressures were monitored by pressure gauges. The downstream pressure (that in the chamber) was regulated at 760 Torr by an adjustable valve installed in the bypass pumping line. A ‘no-flow’ case was also studied, in which the gas was directed into the chamber instead of flowing through the channel between the two electrodes. A direct current power source was used to generate a discharge in the confined slot geometry. The discharge voltage was measured across the electrodes using a high-voltage probe, and the discharge current was derived from the voltage drop across a ‘current-view’ resistor. To measure the electrode temperature, a type-K thermocouple (0.001 in. diameter) was attached with thermally conductive glue on the top surface of each electrode, 2 mm from the surface facing the plasma.

Plasma emission was acquired with an optical emission spectroscopy (OES) setup with $7\times$ magnification optics, a 0.55 m focal length monochromator and a CCD detector, providing a 0.033 nm spectral resolution with a $40 \mu\text{m}$ entrance slit width. This ensemble was described in a previous publication [12]. The spatial resolution of the optical system across the $200 \mu\text{m}$ gap (x -direction in figure 1) between the two electrodes was $\sim 6 \mu\text{m}$.

2.1. Gas temperature measurements

Spatially resolved gas temperatures in the microplasma channel between the two electrodes were deduced from analysis of the emission spectra of the $\text{N}_2 C^3\Pi_u \rightarrow B^3\Pi_g$ second positive system [15]. A small amount of N_2 (typically 0.1%) was added to the main gas feed, and the rotational temperature, T_r , of N_2 was determined by comparing the measured emission spectrum with a simulated spectrum, using the spectroscopic constants of the transition [16], with temperature as the adjustable parameter. The simulated spectrum was generated by computing the positions and intensities of P, Q and R-branch transitions, broadening each of these emission lines over the instrumental resolution and then summing the intensities in discretized wavelength bins. A detailed description of this treatment is given in a previous publication [12].

Equating the rotational temperature $T_r(C)$ of the C state or $T_r(X)$ of the ground state ($X^1\Sigma_g$) with T_g is valid under several classes of conditions, as summarized in the flow chart in figure 2 and parsed as follows:

(a) If the time, $\tau(C)_{R-T}$, for rotational-to-translational (R–T) energy transfer between all populated rotational levels J' of $\text{N}_2(C)$ and the host gas atoms is much shorter than the lifetime of the C state, $\tau(C)$, then the rotational population of the C state thermalizes (resulting in a Maxwell–Boltzmann distribution) before emission occurs and $T_g = T_r(C)$. $\tau(C)$ for the C state

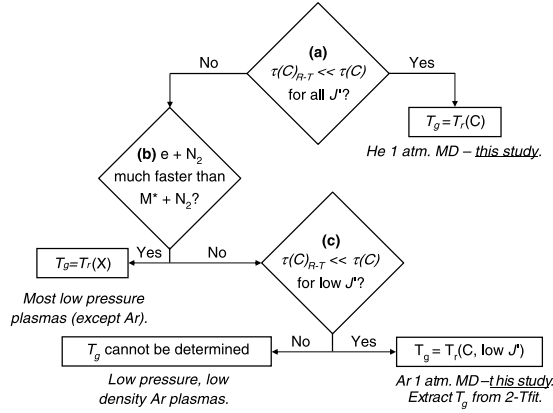


Figure 2. Flow chart indicating which conditions apply in the determination of gas temperature, T_g , from the N_2 ($C^3\Pi_u \rightarrow B^3\Pi_g$) emission bands. $\tau(C)$ is the lifetime of the N_2 ($C^3\Pi_u$) state, including quenching, $\tau(C)_{R-T}$ is the time for C-state rotation to gas translation thermalization, $T_r(C)$ and $T_r(X)$ are the C-state and ground state rotational temperatures, respectively, and J' is the rotational quantum number for the C state.

is given by $\tau(C)^{-1} = \tau_{\text{rad}}^{-1} + \tau_Q^{-1}$, where τ_{rad} is the radiative lifetime (37 ns for the $v' = 0$ vibrational level [15]) and τ_Q^{-1} is the reciprocal of the total first order quenching rate due to collisions with electrons, N_2 or the rare gas (He or Ar). For an electron density of $\sim 10^{13} \text{ cm}^{-3}$ and a reasonable quenching cross-section of $\sim 10^{-15} \text{ cm}^2$, $\tau_Q^{-1} \sim 10^6 \text{ s}^{-1}$ for an electron temperature of 2 eV, i.e. τ_Q is much slower than τ_{rad} . The electronic quenching rate by N_2 is also negligible (10^5 s^{-1}); the quenching rate coefficient for N_2 $C^3\Pi_u$, $v' = 0$ is $1.3 \times 10^{-11} \text{ cm}^3 \text{ s}^{-1}$ [17, 18] and the N_2 number density in the present study was only 10^{16} cm^{-3} . Quenching rate coefficients for rare gases could not be found, but they should be at least an order of magnitude smaller than that for N_2 ; hence, the estimated quenching rate by He or Ar is not likely to exceed 10^7 s^{-1} at atmospheric pressure. Therefore, $\tau(C)$ should be close to its radiative lifetime.

As discussed below, under the experimental conditions of this work, the time for thermalization of the rotational distribution of the C state is expected to be $< 10^{-7} \text{ s}$ for low J' levels, but $> 10^{-7} \text{ s}$ for high J' levels. Thus, collisional transfers among rotational levels of the C state cannot lead to thermal equilibrium between high ($J' > 30$) and low ($J' < 10$) rotational levels. Atmospheric pressure He microdischarges at relatively low gas temperatures, in which only the low J' levels of the C state are substantially populated by electron impact from the ground state of nitrogen, fall in this category. For such microdischarges, the N_2 ($C^3\Pi_u$, $v' = 0 \rightarrow B^3\Pi_g$, $v'' = 2$) transition was found to have minimal spectral interference from background emissions from He, He_2 and trace impurities and was used to measure the gas temperature [12]. (Throughout the paper, the superscripts prime and double prime refer to upper and lower electronic states, respectively.) If (a) is false, then:

(b) If direct electron impact excitation from the ground state $N_2(X^1\Sigma_g)$ is the dominant excitation mechanism of the C state, then $T_g = T_r(X)$. N_2 in its ground electronic and vibrational state can be excited to all accessible vibrational levels of the $C^3\Pi_u$ state by collisions with electrons:

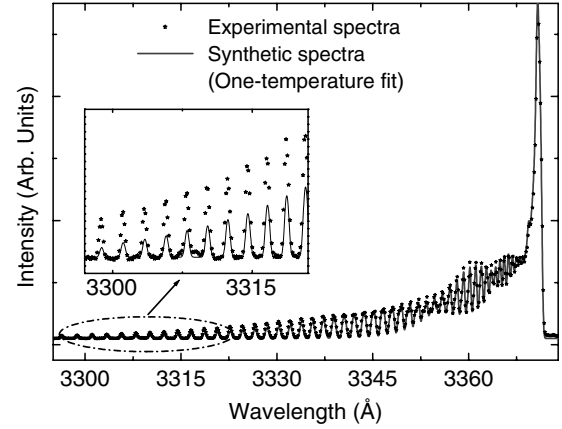
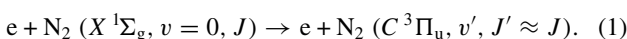
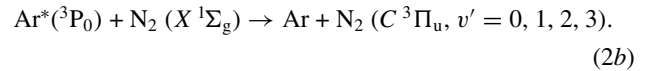
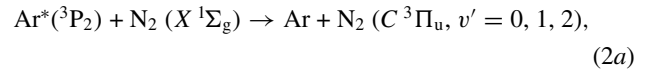


Figure 3. A sample of observed and synthetic spectra of the N_2 ($C^3\Pi_u$, $v' = 0 \rightarrow B^3\Pi_g$, $v'' = 0$) transition in Ar/0.1% N_2 dc microplasmas at 760 Torr, based on the one-temperature fitting method. The magnified part shows the discrepancy between the synthetic and the observed spectra as a result of neglecting excitation to the high J' levels of the C state by energy transfer between metastable Ar^* and N_2 (see text).

Due to the long residence time of N_2 in the plasma, the $N_2(X)$ state is in rotational–translational equilibrium with the host gas. Since the change in rotational angular momentum is small during electron impact excitation, the ground state rotational distribution is transferred to the $N_2(C)$ state. Low pressure (< 1 Torr) discharges that do not contain large fractions of Ar generally fall under this category [15].

For plasmas that contain large amounts of Ar, however, excitation of N_2 by energy transfer from Ar metastable atoms can also take place:



It was shown in [19] that at room temperature, the most abundant $\text{Ar}^*(^3P_2)$ metastable atoms populate the $v' = 0$, 1 and 2 levels of the N_2 C state, while the 0.15 eV higher energy $\text{Ar}^*(^3P_0)$ metastable atoms populate the $v' = 0$, 1, 2 and 3 levels. Based on measurements in the afterglow of a pulsed Ar/ N_2 discharge [20], or in the flowing afterglow of an Ar discharge with N_2 added downstream [21], it was reported that energy transfer from Ar^* to N_2 resulted in preferential population of high rotational levels (up to $J' = 55$) of the N_2 $C^3\Pi_u$, $v' = 0$ state, with an effective ‘rotational temperature’ of about 2300 K [20, 21].

In high charge density, low pressure Ar discharges (e.g. inductively coupled Ar plasma at 10 mTorr [22]), reaction (1) is fast compared with reactions (2a) and (2b), N_2 emission spectra are well represented by a Boltzmann distribution, and case (b) in figure 2 is true. Conversely, it appears that in atmospheric pressure Ar microdischarges, contributions from reactions (2a) and (2b) exceed those from electron impact excitation, and case (b) in figure 2 is false. Evidence for this is contained in figure 3, which shows that when an acceptable fit was obtained for the long wavelengths (emission from low J' levels of the $C^3\Pi_u$ $v' = 0$ state), the one-temperature synthetic

spectrum predicted a much reduced emission intensity (see inset of figure 3) for the short wavelengths (emission from high J' levels). This overpopulation of high J' levels is attributed to reactions (2a) and (2b). Additional evidence comes from the observation that emission from $v' = 3$ and 4 is extremely weak relative to emission from $v' = 0, 1$ and 2.

Since the rotational angular momentum of the molecule is preserved in reaction (1), the low rotational levels of the N_2 ($C^3\Pi_u$) state are preferentially populated if the gas is relatively cool. For example, the rotational population peaks at $J' \cong 9$ for $T_g = 500$ K. To extract T_g from the N_2 emission spectrum under these conditions, R–T energy transfer in collisions between N_2 ($C^3\Pi_u$) and Ar must be fast for the low J' levels.

Many studies have been carried out to measure the state-to-state rotational transfer in excited states of diatomic molecules, due to collisions with various rare gas atoms and molecules, such as He, Ar, N_2 and H_2 [23–26]. The total rotational collision cross-section was found to range between $\sim 10^{-15}$ and $\sim 10^{-14}$ cm^2 , which at atmospheric pressure would correspond to collisional frequencies of about 10^9 s^{-1} or larger. This is much higher than the 2.7×10^7 s^{-1} radiative decay frequency, indicating that N_2 $C^3\Pi_u$ will undergo multiple rotationally inelastic collisions during its lifetime at atmospheric pressure. However, the state-to-state rotational transfer rate coefficients, $k_{if}(J_i \rightarrow J_f)$, from an initial level J_i to a final level J_f decrease with increasing J_i and energy difference between initial and final rotational states, $\Delta E_{if} = |F_{J_i} - F_{J_f}|$, where F_J is the rotational energy of the J level. Several scaling laws have been proposed [23–28], including the power decay law, $k_{if} \propto \Delta E_{if}^{-\gamma}$, where γ is a positive constant. Given that $\Delta E_{if} \cong 2BJ_i\Delta J$ (where B is the rotational constant) and $\gamma \approx 1$ [23, 24], the rate coefficient out of the J_i level scales approximately as $1/(J_i\Delta J)$. Thus, the state-to-state rate coefficient is large for small J_i and small ΔJ . In addition, the total rotationally inelastic rate coefficient out of the J_i level, $\sum_{J_f} k_{if}$, is higher for smaller rotational numbers J_i [26, 29], since there is a wider availability of J_f levels because of the small energy gaps.

Therefore, the population of the low J' levels of the N_2 ($C^3\Pi_u$, $v' = 0$) state in atmospheric pressure Ar plasmas should obey a Maxwell–Boltzmann distribution with $T_g = T_r(C, \text{low } J')$, but the high J' levels should be overpopulated, on account of reactions (2a) and (2b). Even if the low J' levels do not undergo a sufficient number of thermalizing collisions with Ar, $T_g = T_r(C, \text{low } J')$ is a good assumption, since the low J' levels are populated to a significant degree by electron impact excitation of ground state N_2 , for which R–T equilibrium is established. Therefore T_g will lie between $T_r(C, \text{low } J')$ and $T_r(X)$, but since the rotational constants of the ground state and the $C^3\Pi_u$ state are nearly the same, $T_r(C, \text{low } J') \approx T_r(X)$.

Conversely, N_2 ($C^3\Pi_u$, $v' = 0$) in high J' levels formed by energy transfer from Ar metastable atoms will not undergo a significant angular momentum loss and the population distribution of these high J' levels will retain the memory of their initial ' T_r ' which is about 2300 K. Therefore, case (c) in figure 2 is true, requiring a two-temperature fit to the observed spectrum. The rotational population $[N_J]$ may

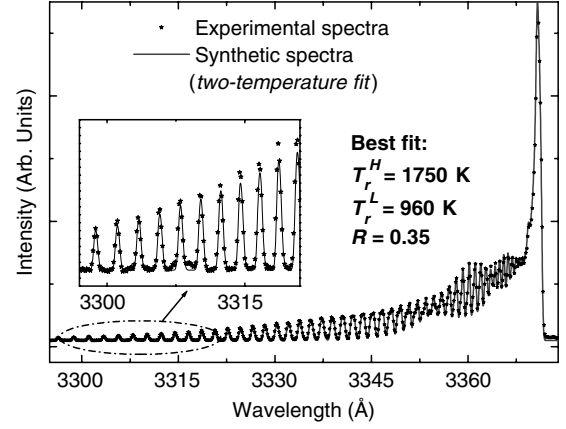


Figure 4. A sample of observed and synthetic spectra of the N_2 ($C^3\Pi_u$, $v' = 0 \rightarrow B^3\Pi_g$, $v'' = 0$) transition in Ar/0.1% N_2 dc microplasmas at 760 Torr, based on the two-temperature fitting method (see text). The magnified part shows much better agreement between the two spectra as compared with that in figure 3.

then be represented by

$$[N_J] \propto (2J + 1) [\exp(-F_J/kT_r^L) + R(T_r^L/T_r^H) \exp(-F_J/kT_r^H)], \quad (3)$$

where F_J is the rotational energy, T_r^L and T_r^H are temperatures corresponding to two individual Maxwell–Boltzmann distributions and R is the fraction of the high temperature population. T_r^L would thus correspond to the distribution of low J' levels, for which the R–T equilibrium is effective with $T_r^L = T_g$, and T_r^H , which has no particular physical meaning, represents the distribution of high J' levels that suffered a few rotational cascades after formation by energy transfer from Ar metastables. The validity of equation (3), i.e. the bimodal population distribution of N_2 (C , $v' = 0$) in Ar/ N_2 atmospheric pressure plasmas, was verified with a simple collisional–radiative model which used a realistic set of state-to-state rotational transfer coefficients k_{if} and the known initial distributions in the J' levels by energy transfer [20].

Figure 4 shows a fit of the observed N_2 (C , $v' = 0 \rightarrow B$, $v'' = 0$) spectra with a synthetic spectrum using the two-temperature distribution. The experimental spectrum is the same as in figure 3. The three parameters T_r^H , T_r^L and R in equation (3) were determined using a nonlinear fitting procedure (Levenberg–Marquardt method, see [30]), by minimizing χ^2 . In contrast to the one-temperature fit, the ‘two-temperature’ fit clearly demonstrates much better agreement over the whole wavelength range. The best fit to the experimental data was obtained with $T_r^L = 960$ K, $T_r^H = 1750$ K and $R = 0.35$.

It should be noted that in Ar/ N_2 plasmas, the $v' = 3$ and $v' = 4$ levels of the N_2 $C^3\Pi_u$ state are populated predominantly by electron impact excitation, since energy transfer from Ar metastable atoms is not effective for these levels. Therefore, a simpler way to determine the gas temperature would be to fit the 3–3 and 4–4 emission bands with one rotational temperature, T_r , as was done in [22]. Under the experimental conditions of this work, however, these bands were very weak and were plagued by spectral interferences.

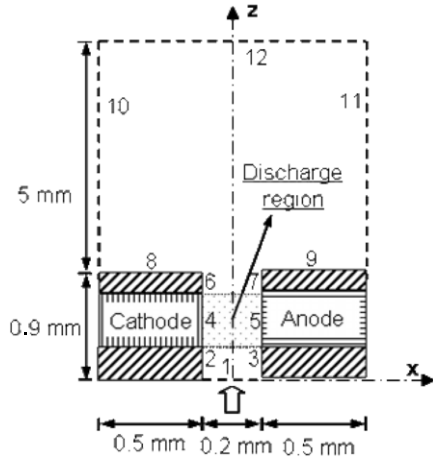


Figure 5. Schematic of the computational domain for the two-dimensional gas flow dynamics model. The gas enters at the bottom of the channel, flows through the discharge region and then into the open space downstream.

The error in gas temperature measurement was estimated to be ± 10 K for the one-temperature fit applied to He/N₂ plasmas, and ± 40 K for the T_r^L values derived from the two-temperature fit applied to Ar/N₂ plasmas. The fitted temperature values can vary within these error bands depending on the wavelength range used for the fit, and the location of the baseline of the spectra.

2.2. Description of plasma-gas dynamics model

A plasma-gas dynamics model was employed to study the effect of gas flow on gas temperature in the microplasma channel. The helium plasma was described by a one-dimensional self-consistent fluid model which included the mass continuity equations for charged (e^- , He⁺ and He₂⁺) and neutral species (ground and metastable states of He, and the metastable He₂), the electron energy equation and Poisson's equation for the electric field. The plasma chemistry set included reactions deemed to be important in high pressure discharges (Penning-ionization, dissociative recombination, collisional-radiative recombination, radiation trapping, etc). A conductive heat transport equation for the working gas was also incorporated. A detailed description of the helium plasma model can be found in [31]. The plasma model was applied to dc microplasma discharges with no convective flow through the discharge region (i.e. for the 'no-flow' case). A recent update of the model included Ar plasma chemistry at high pressure, so that the model can also be applied to Ar microplasma discharges [32]. The measured electrode temperature (assumed to be the same as the gas temperature at the wall) was used as the boundary condition for the gas temperature equation.

Figure 5 shows a schematic of the computational domain (Cartesian coordinates) used in this study. The geometry included the gas inlet region, the discharge region and the downstream region. The gas (He or Ar) flowed from the bottom to the top in figure 5, and the discharge was struck in the channel between the two electrodes. The gas dynamics model was based on the following assumptions:

- (1) Since the length of each electrode (6 mm) was much larger than either the electrode height (0.5 mm) or the

channel width (0.2 mm), the system was assumed to be two-dimensional (i.e. variables change only in the x and z directions in figure 5).

- (2) Since the Reynolds number in the channel, Re , was estimated to be in the range 10–300, gas flow was assumed to be laminar.
- (3) Since the Knudsen number, Kn ($=\lambda/d$, where λ is the gas mean free path, and d is the channel width) was less than 0.001, the gas was treated as continuum. Gas rarefaction should become important when $0.001 < Kn < 0.1$, and this can cause velocity slip and temperature jumps at the wall.
- (4) The maximum Mach number in the channel, Ma ($=v/\sqrt{1.67RT/M}$, where v is the fluid velocity and M is the gas molar mass), was ~ 0.20 . Hence, gas flow was subsonic. A compressible fluid dynamics model was used since studies of gas flow in microchannels [10] have shown that gas compressibility effects become important for Ma greater than ~ 0.2 .
- (5) The addition of small amounts of N₂ (0.1%) was assumed to have no effect on the plasma chemistry. The model was therefore set for pure He or Ar.
- (6) The fluid was assumed to obey the ideal gas law.
- (7) The system was assumed to be in steady state.

Based on the above assumptions, the governing equations for gas flow are as follows:

Continuity of mass:

$$\frac{\partial(\rho u)}{\partial x} + \frac{\partial(\rho v)}{\partial z} = 0, \quad (4)$$

where ρ is the density of the gas, and u and v are the velocities in the x and z directions, respectively.

Conservation of x -momentum:

$$\frac{\partial(\rho u^2)}{\partial x} + \frac{\partial(\rho uv)}{\partial z} = -\frac{\partial P}{\partial x} - \left(\frac{\partial \tau_{xx}}{\partial x} + \frac{\partial \tau_{zx}}{\partial z} \right) + F_x. \quad (5)$$

Conservation of z -momentum:

$$\frac{\partial(\rho v^2)}{\partial z} + \frac{\partial(\rho uv)}{\partial x} = -\frac{\partial P}{\partial z} - \left(\frac{\partial \tau_{zz}}{\partial z} + \frac{\partial \tau_{xz}}{\partial x} \right) + F_z, \quad (6)$$

where P is pressure, and τ_{xx} , τ_{xz} , τ_{zx} and τ_{zz} are the corresponding components of the viscous stress tensor, $\bar{\tau}$. For Newtonian fluids, these components are [33],

$$\tau_{xx} = -\mu \left[2 \frac{\partial u}{\partial x} - \frac{2}{3} \left(\frac{\partial u}{\partial x} + \frac{\partial v}{\partial z} \right) \right], \quad (7a)$$

$$\tau_{zz} = -\mu \left[2 \frac{\partial v}{\partial z} - \frac{2}{3} \left(\frac{\partial u}{\partial x} + \frac{\partial v}{\partial z} \right) \right], \quad (7b)$$

$$\tau_{xz} = \tau_{zx} = -\mu \left(\frac{\partial u}{\partial z} + \frac{\partial v}{\partial x} \right), \quad (7c)$$

where μ is the viscosity of the gas. In equations (5) and (6), F_x and F_z represent the volume force $\vec{F} = (F_x, F_z)$ as a result of momentum transfer from the charged particles to the gas in

the x and z directions, respectively [11]:

$$F_x = \sum_i q_i N_i E_x, \quad (8a)$$

$$F_z = \sum_i q_i N_i E_z, \quad (8b)$$

where the force $\vec{F} = (F_x, F_z)$ is the sum over all charged species (including electrons, atomic and molecular ions) having density N_i , and charge q_i , in the electrostatic field $\vec{E} = (E_x, E_z)$. Equations (8a) and (8b) ignores small contributions to the force due to charged particle gradients (see also discussion in [33]). The buoyancy force was ignored in the momentum conservation equations.

Equations (8a) and (8b) indicate that the volume forces F_x and F_z may play a significant role in the momentum equations in regions of high electric field. Hence, in the microplasma configuration used in this study, F_x may be important in the cathode sheath region, but F_z should be relatively small, because the electric field in a direction parallel to the electrode surfaces (z -direction) is small.

Conservation of energy [33]:

$$\rho C_p \left(u \frac{\partial T}{\partial x} + v \frac{\partial T}{\partial z} \right) = \left[\frac{\partial}{\partial x} \left(k \frac{\partial T}{\partial x} \right) + \frac{\partial}{\partial z} \left(k \frac{\partial T}{\partial z} \right) \right] + \left(u \frac{\partial P}{\partial x} + v \frac{\partial P}{\partial z} \right) + \mu \Phi + P_g. \quad (9)$$

In the above equation, the left hand side represents energy transport by convection. The terms on the right hand side represent, in the order shown, energy transport by conduction, reversible energy conversion by fluid expansion/compression, irreversible energy conversion by viscous dissipation, and gas heating by the plasma, respectively. Heat exchange due to thermal radiation is negligible, because the gas is mainly atomic, which neither absorbs nor emits thermal radiation. For Newtonian fluids, the viscous dissipation function Φ is given by [34]

$$\Phi = 2 \left(\frac{\partial u}{\partial x} \right)^2 + 2 \left(\frac{\partial v}{\partial z} \right)^2 + \left(\frac{\partial u}{\partial z} + \frac{\partial v}{\partial x} \right)^2 - \frac{2}{3} \left(\frac{\partial u}{\partial x} + \frac{\partial v}{\partial z} \right)^2. \quad (10)$$

In the microplasma discharge, a significant fraction of the input power is dissipated in gas heating. As discussed before [31], ion Joule heating is the dominant gas heating mechanism at atmospheric pressure, resulting in $P_g = \vec{j}_+ \cdot \vec{E}$, where \vec{j}_+ is the ion (atomic + molecular) current. To calculate the heating source P_g in the gas energy equation, and the volume force \vec{F} in the momentum equation, one requires information on plasma properties, such as the electric field, and the number densities of the positive ions and electrons. These were obtained from the plasma model, and are generally expected to change with gas flow rate, i.e. the plasma model and the gas dynamics model should be coupled together. However, under constant power input (i.e. constant IV), P_g and \vec{F} should not be affected significantly by gas flow. Thus, use of these properties from the (no-flow) plasma model in the gas dynamics model in a decoupled manner should yield reasonable results for the gas temperature distribution.

Boundary conditions for the governing equations included: (1) at the channel inlet (boundary 1 in figure 5),

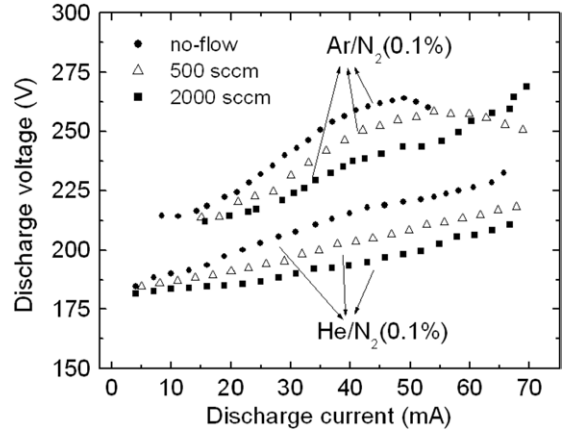


Figure 6. I - V characteristics of dc microdischarges in He/0.1%N₂ and Ar/0.1%N₂ used in this study.

a fully developed flow in the z -direction (parabolic profile) was used. The corresponding average velocity, v_0 , was calculated from the gas flow rate, the cross section of the channel, and the upstream pressure using a temperature of 300 K; (2) on the sidewalls of the channel (boundaries 2–7), a no-slip condition was applied for velocity, and the electrode temperature was obtained from the thermocouple measurements; (3) on the top surfaces of the slot (boundaries 8 and 9), a no-slip condition was again used for velocity, and the temperature profile was linearly interpolated from the electrode temperature to 300 K; (4) for the downstream region, the velocity gradient in the normal direction was set equal to zero (e.g. $\partial u/\partial z = \partial v/\partial z = 0$) on boundary 12, while $\partial u/\partial x = 0$ and $v = 0$ for boundaries 10 and 11; (5) the gas temperature was set at 300 K at the downstream boundaries 10 and 11, while a convective heat flux-dominated boundary condition was applied at boundary 12. The pressure was taken to be 760 Torr at the top of the computational domain. A reference pressure is necessary to calculate the gas density from the ideal gas law. The boundary conditions used in this work were similar to those applied in a plasma torch simulation [35]. To account for the widely varied gas temperature, the physical and transport properties of the gas, such as density, thermal conductivity and viscosity, were expressed as a function of temperature.

The model equations were solved using FEMLAB (Comsol Multiphysics), a partial differential equation solver based on a Finite Element Method. A streamline upwind Petrov-Galerkin formulation [36], which adds an anisotropic diffusion term in the direction of flow, was selected to handle the highly convective cases.

3. Results and discussion

Figure 6 shows the current–voltage (I - V) characteristics of dc microplasma discharges in both helium and argon (each with 0.1% by volume added nitrogen) at atmospheric pressure. For each gas, measurements were made for three different flow rates. Both He and Ar discharges were operated in an abnormal glow discharge mode, as indicated by the positive slope of the I - V curves, except for Ar microplasmas at high discharge voltage and low flow rates. In contrast to argon, helium microdischarges exhibit I - V curves of a smaller slope

Table 1. Experimental conditions and selected experimental results.

	Case 1(a)	Case 1(b)	Case 1(c)	Case 2(a)	Case 2(b)	Case 2(c)
Working gas		He + N ₂ (0.1%)			Ar + N ₂ (0.1%)	
Downstream pressure (Torr)		760			760	
Flow rate (sccm) ^a	'No-flow'	500	2000	'No-flow'	500	2000
Discharge current (mA)	54.1	55.6	57.9	46.0	47.5	48.7
Current density (mA cm ⁻²) ^b	1803	1853	1930	1533	1583	1623
Discharge voltage (V)	222	217	206	262	255	244
Input power (W)	12.0	12.1	11.9	12.0	11.8	11.9
Power density (kW cm ⁻³) ^c	~20	~20	~20	~20	~20	~20
Cathode temperature (K)	507	486	445	713	693	621
Anode temperature (K)	415	405	363	455	436	418
Averaged bulk gas temperature (K)	595	545	480	940	801	603
Pressure drop (Torr)						
With plasma	0	0.4	2.0	0	1.4	6.9
Without plasma	0	0.3	1.6	0	0.9	4.6

^a 'No-flow' here means there was no forced convective flow through the microplasma channel.

^b Under the condition of a dc abnormal glow discharge, the current density was estimated from the discharge current divided by the electrode area.

^c Power density was estimated from the total input power divided by the channel volume between the two electrodes.

over a wider operating range and smaller operating voltage for the same discharge current. A tendency for glow-to-arc transition is shown by the Ar microplasma at ~50 mA with no gas flow or 500 sccm through the channel. Figure 6 also indicates that increasing the gas flow generally results in a slightly lower discharge voltage for both plasmas. Moreover, gas flow through the Ar microplasma seems to delay the glow-to-arc transition and can therefore extend the operating window for a stable microdischarge. For the same discharge current, introduction of 0.1% N₂ to nominally pure He or Ar (UHP grade, impurity <10 ppm) discharges caused an increase of about 10% in the discharge voltage (not shown). Nevertheless, the shape of the *I*-*V* curves was nearly the same as shown in figure 6. An amount of 0.1% of N₂ addition was necessary to have sufficient signal-to-noise ratio to perform OES measurements of gas temperature.

Table 1 lists the experimental parameters used for the two gases studied. For each gas, three cases were examined: (a) no-flow, (b) 500 sccm and (c) 2000 sccm. In order to make comparisons, the input power density was kept constant (~20 kW cm⁻³) for all cases. Figures 7(a) and (b) show spatially resolved measurements of gas temperature in He and Ar microplasmas, respectively, for the experimental conditions listed in table 1. For both argon and helium gases, the temperature profile is highly non-uniform across the microdischarge gap, with the temperature peaking near the cathode. This is because ion Joule heating, which was found to be the major gas heating mechanism in atmospheric pressure dc discharges, is limited to the vicinity of the cathode. Because helium has a much higher thermal conductivity than argon ($1.6 \times 10^{-3} \text{ J cm}^{-1} \text{ s}^{-1} \text{ K}^{-1}$ in He versus $1.8 \times 10^{-4} \text{ J cm}^{-1} \text{ s}^{-1} \text{ K}^{-1}$ in Ar at 300 K), the resulting bulk gas temperature in He microplasmas is only ~600 K for the no-flow case, which is much lower than the corresponding bulk gas temperature of ~940 K in argon. Under constant input power, gas flow through the microplasma channel results in lower gas temperature for both gases. As the gas flow rate increases, the cooling effect becomes more significant, causing the bulk gas temperature to drop from ~600 K at no-flow to ~480 K at 2000 sccm for He, and from ~940 K to ~600 K

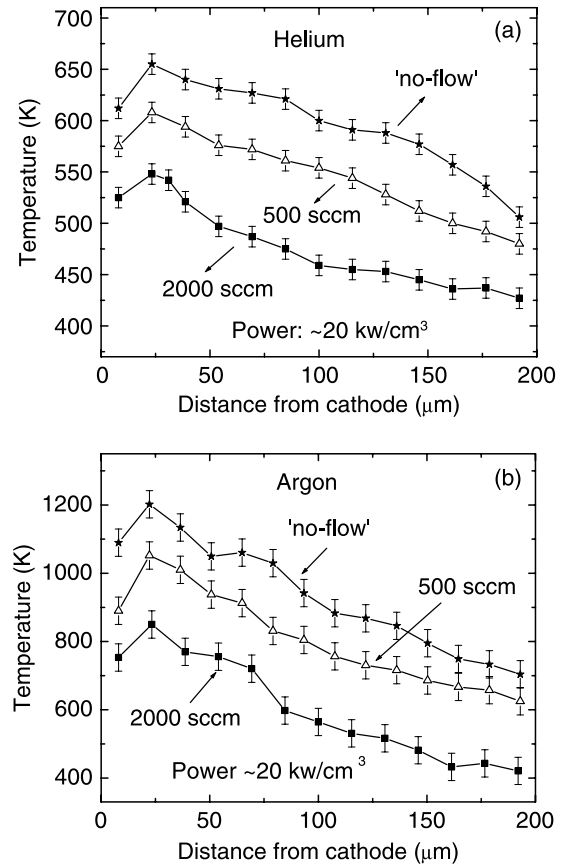


Figure 7. Spatially resolved gas temperature profiles across the channel of dc microplasmas at $P = 760$ Torr as a function of gas flow rate for (a) He/0.1%N₂ and (b) Ar/0.1%N₂ discharges.

for Ar, respectively. It should be noted that the measured gas temperatures in He microplasmas for the no-flow case are a bit higher than those reported previously [12]. The higher temperatures in the current work are due to the thicker electrodes (500 μm versus 100 μm in the previous study).

The gas temperature profiles shown in figure 7 reflect the combined influence of gas heating by the plasma and cooling

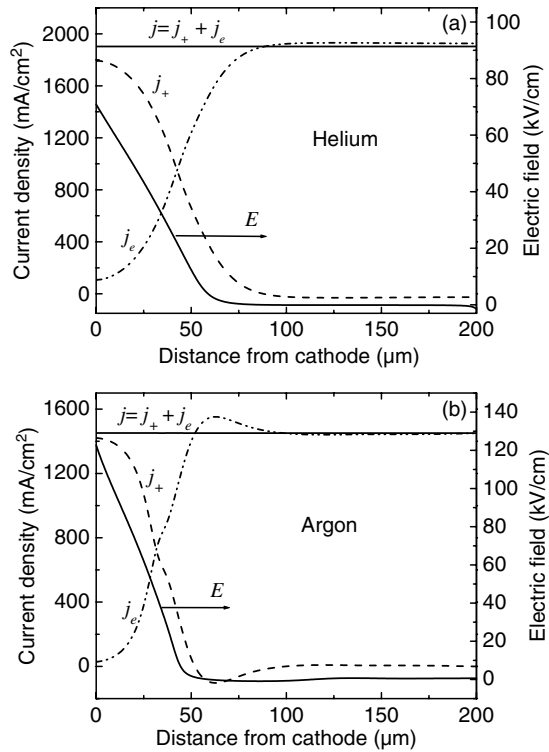


Figure 8. Simulation results of electric field E and current density profiles (including ion current density j_+ , electron current density j_e and total current density $j = j_+ + j_e$) for dc microplasmas with ‘no-flow’ in (a) helium and (b) argon.

by gas convection and conduction. To understand the interplay of these effects, simulations using the plasma-gas dynamics model were performed under the same conditions as in the experiments. A selection of predicted plasma properties obtained from the plasma model for He and Ar microplasmas, including ion current density j_+ , electron current density j_e , total current density $j (= j_+ + j_e)$, and electric field E profiles, is shown in figures 8(a) and (b). As expected, the total discharge current was independent of position for both gases. The ion current dominates the electron current in the cathode fall while, in the rest of the discharge, almost all current is carried by electrons. The electric field peaks at the cathode surface and decreases monotonically to very small values in the bulk. The plasma simulation revealed that (under the conditions of figure 8) 87% of the total input power in the He discharge and 84% of the total input power in the Ar discharge end up heating the gas.

It should be noted that besides gas heating, the so-called ‘ion pumping’ effect (the result of momentum transfer from plasma ions to the neutral gas) may also play an important role in the gas dynamics. Kushner [11], in his calculations of the plasma and gas properties in a microplasma source, showed that the body force from charged particles on the neutral gas can generate gas flow at speeds up to 23 m s^{-1} on the axis of the channel without an externally impressed pressure gradient. The ion pumping effect was analysed in this study by comparing the simulation results with and without the body force F term in equations (5) and (6). For the parallel-plate configuration of the microplasma source used in this work, ion pumping was found not to have an important influence on the

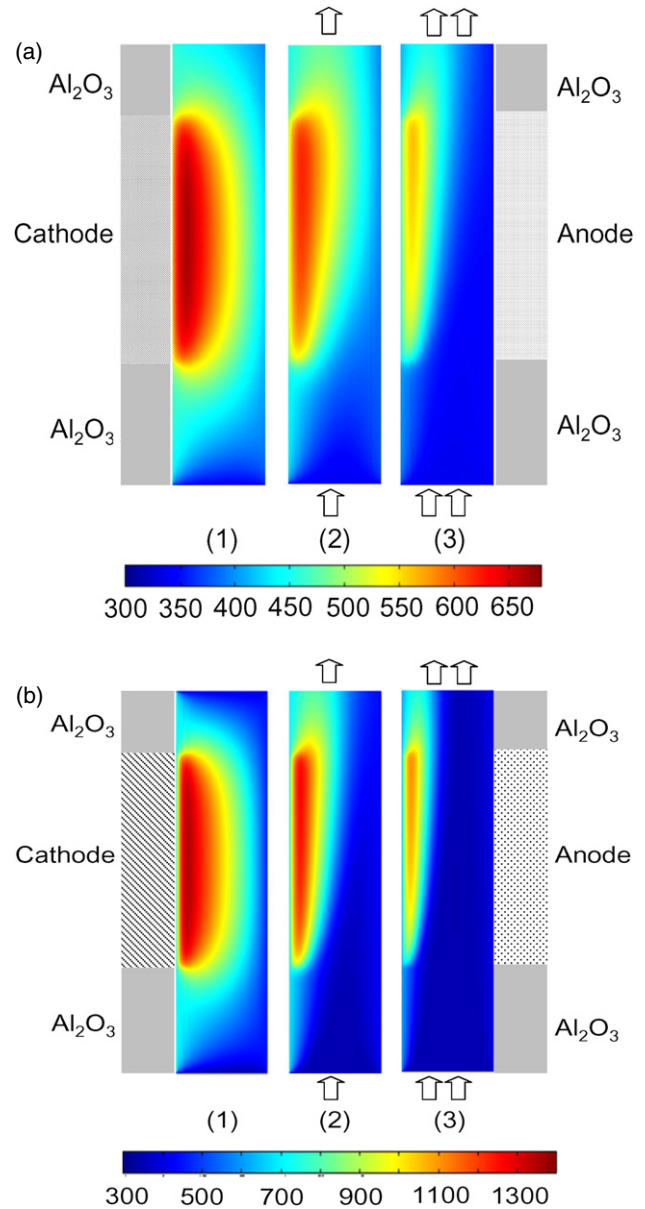


Figure 9. Simulation results of two-dimensional profiles of gas temperatures in dc microplasma discharges in (a) helium and (b) argon, under three cases of gas flow: (1) no-flow, (2) 500 sccm and (3) 2000 sccm.

(This figure is in colour only in the electronic version)

gas temperature profiles. This is because, in contrast to [11], the electric field (therefore the body force, F) is strongest in the horizontal x -direction (perpendicular to the electrodes), while the main gas flow is in the vertical z -direction.

Figures 9(a) and (b) show the two-dimensional gas temperature distributions in the microdischarge region for helium and argon gas, respectively. For both cases, the gas temperature in the microplasma channel decreases as the gas flow rate increases. For the ‘no-flow’ case, the gas temperature peaks near the cathode and the profiles are nearly symmetric with respect to the horizontal plane through the middle of the electrodes. For the high flow rate case, higher temperatures are established further upstream, as a result of convective heat transport by the flowing gas. It is also clear that the gas

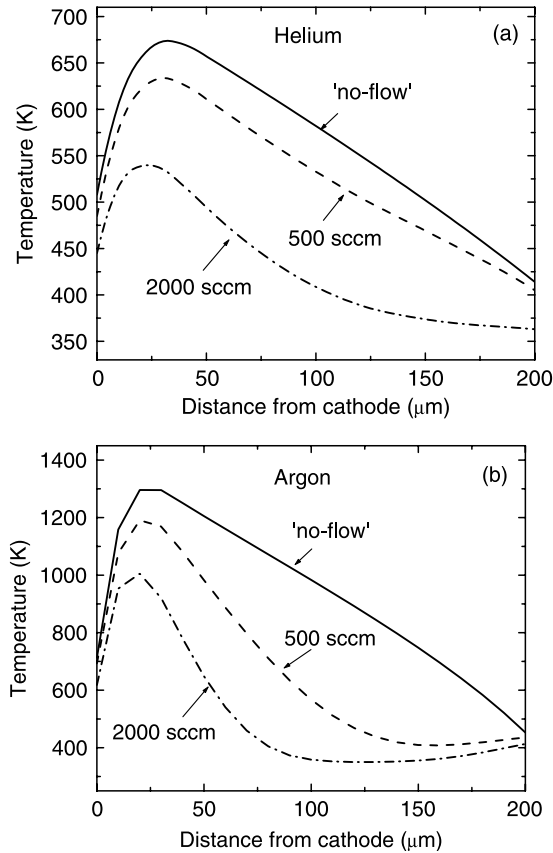


Figure 10. Simulation results of gas temperature profiles across the channel between the two electrodes as a function of gas flow rate for (a) helium and (b) argon gas. The plots were obtained by averaging the 2D temperature profiles (shown in figure 9) in the z -direction.

temperature in helium is much cooler compared with that in argon, as found experimentally.

A direct comparison between the essentially one-dimensional experimental measurements with the two-dimensional theoretical predictions is difficult. This is because the experimental results presented in figure 7 in fact reflect average gas temperature profiles. Spatial averaging occurs both along the optical axis (z -direction) as well as in the horizontal direction. To deduce the contribution to the measured point-wise optical emission intensity of different discharge regions, one would require detailed information about the optical system (such as depth of focus) as well as the spatial distribution of plasma emission originating from the species of interest. Despite these difficulties, one can still make a qualitative comparison with the measurements by simply averaging the predicted 2D temperature profiles along the optical axis (z -direction), assuming uniform optical intensity and a homogenous plasma in that direction. The derived 1D gas temperature profiles for helium and argon are presented in figures 10(a) and (b), respectively.

Comparison between figures 10 and 7, suggests that the model predicts the experimental results reasonably well, especially considering the fact that there were no adjustable parameters used in the model. For example, the model predicts the maximum temperature value and its location between the two electrodes, the trend of decreasing temperature with increasing gas flow rate, and the significant temperature

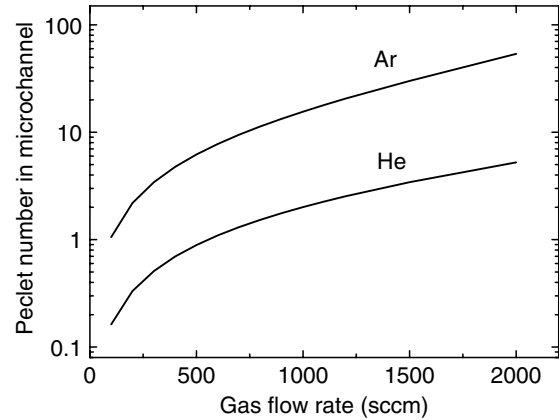


Figure 11. Peclet number in the channel of the microplasma source as a function of flow rate for (a) helium and (b) argon gases.

differences between helium and argon under the same conditions of input power and flow rate. The agreement between the measurements and the theoretical predictions may be improved by a self-consistent simulation where the plasma and gas dynamics are solved in a coupled manner.

As shown in table 1 and figure 7, gas flow in argon microplasmas has a greater cooling effect compared with helium microplasmas. As an example, the average bulk gas temperature in argon drops by ~ 340 K from the 'no-flow' case to the 2000 sccm case, compared with a ~ 110 K drop in helium. To further explain the significant differences between these two gases, the dimensionless Peclet number, Pe , widely used in classical heat transport analyses [34], was calculated as a function of a flow rate for both gases. The Peclet number shows the relative importance of heat transport by convective gas flow as compared with heat transport by conduction. Here, $Pe = l_0 v_0 / \alpha$, where l_0 is a characteristic length of the microchannel (taken here as the half-width of the channel), v_0 is the average flow velocity in the microchannel and α is the thermal diffusivity of the gas (at the average bulk temperature). The result is shown in figure 11. Since Pe for helium is relatively small (≤ 5), even for flow rates up to 2000 sccm, heat transport by conduction is dominant in helium compared with heat transport by convection. Thus, convective gas flow does not have a pronounced effect. The reverse is true in the case of argon, for which Pe is as high as ≥ 50 , indicating that convective heat transport is dominant, and gas flow should have a significant effect on gas temperature.

Table 1 also lists the measured pressure drop across the microchannel with the downstream (chamber) pressure kept at 760 Torr. For both gases, a higher flow rate yields a larger pressure drop, as expected. Also, the presence of plasma results in a larger pressure drop compared with the no plasma case. This is mainly because of the reduction in gas density (according to the Hagen–Poiseuille equation, the pressure drop is inversely proportional to the gas density for a given mass flow rate, see [34, p 51]).

4. Conclusions

The effect of convective gas flow on gas temperature in a slot-type, atmospheric pressure, dc microplasma was studied.

Helium and argon microplasmas were sustained in a 200 μm wide channel formed by parallel-plate electrodes through which gas was flowing in a laminar, subsonic flow. Spatially resolved gas temperature profiles across the gap between the two electrodes as a function of flow rate were obtained by N_2 rotational spectroscopy. To derive the gas temperature in Ar/N_2 discharges, a 'two-temperature' model of the N_2 ($C^3\Pi_u$, $v' = 0 \rightarrow B^3\Pi_g$, $v'' = 0$) emission spectra was employed in which both electron impart excitation of N_2 and energy transfer by metastable Ar^* to N_2 were taken into account. For both gases, the measured gas temperature peaked near the cathode and decreased with increasing gas flow rate. Under a constant input power density of $\sim 20 \text{ kW cm}^{-3}$, the bulk gas temperature in the helium microdischarge dropped from $\sim 600 \text{ K}$ for the 'no-flow' case to 480 K for a flow rate of 2000 sccm. The corresponding bulk gas temperature in argon microdischarges decreased from 940 K for the 'no-flow' case to $\sim 600 \text{ K}$ at a flow rate of 2000 sccm.

A plasma model was also used to calculate the power and momentum input to the neutral gas and their effect on gas dynamics and heat transport in the microdischarge. The major gas heating mechanisms was ion Joule heating, concentrated in the cathode sheath region. Gas flow had a higher cooling effect in argon compared with helium microplasmas. This was explained by the relative importance of heat transport by convection versus that by conduction (Péclet number). The predicted gas temperature profiles were in good agreement with experimental measurements.

Acknowledgments

The authors would like to thank the Department of Energy for funding support of (Grant No DE-FG02-03ER54713). FD is grateful to the German Science Foundation and the Bavarian Research Foundation for financial support. Many thanks to Dr I Koleva of the University of Sofia, Bulgaria, for fruitful discussions.

References

- [1] Schoenbach K H, Moselhy M, Shi W and Bentley R 2003 *J. Vac. Sci. Technol. A* **21** 1260
- [2] Eden J G, Park S-J, Ostrom N P and Chen K-F 2005 *J. Phys. D: Appl. Phys.* **38** 1644
- [3] Iza F and Hopwood J A 2003 *IEEE Trans. Plasma Sci.* **31** 782
- [4] Kikuchi T, Hasegawa Y and Shirai H 2004 *J. Phys. D: Appl. Phys.* **37** 1537
- [5] Hsu D D and Graves D B 2003 *J. Phys. D: Appl. Phys.* **36** 2898
- [6] Rahman A, Yaline A P, Surla V, Stan O, Hoshimiya K, Yu Z, Littlefield E and Collins G J 2004 *Plasma Sources Sci. Technol.* **13** 537
- [7] Guo Z Y and Wu X B 1996 *Int. J. Mass Heat Transfer* **46** 3251
- [8] Arkilic E B, Schmidt M A and Breuer K S 1997 *J. Microelectromech. Syst.* **6** 167
- [9] Morini G L 2004 *Int. J. Thermal Sci.* **43** 631
- [10] Ji Y, Yuan K and Chung J N 2006 *Int. J. Mass Heat Transfer* **49** 1329
- [11] Kushner M J 2005 *J. Phys. D: Appl. Phys.* **38** 1633
- [12] Wang Q, Koleva I, Economou D J and Donnelly V M 2005 *J. Phys. D: Appl. Phys.* **38** 1690
- [13] Bose D, Govindan T R and Meyyappan M 1999 *J. Electrochem. Soc.* **146** 2705
- [14] Nam S-K, Shin C B and Economou D J 1999 *Mater. Sci. Semicond. Process.* **2** 271
- [15] Donnelly V M and Malyshev M V 2000 *Appl. Phys. Lett.* **77** 2467
- [16] Roux F, Michaud F and Vervloet M 1993 *J. Molecular Spectrosc.* **158** 270
- [17] Dilecce G, Ambrico P F and De Benedictis S 2006 *Chem. Phys. Lett.* **431** 241
- [18] Pancheshnyi S V, Starikovskaia S M and Starikovskii A Yu 2000 *Chem. Phys.* **262** 349
- [19] Sadeghi N, Cheaib M and Setser D W 1989 *J. Chem. Phys.* **90** 219
- [20] Nguyen T D and Sadeghi N 1983 *Chem. Phys.* **79** 41
- [21] Setser D W, Stedman D H and Coxon J A 1970 *J. Chem. Phys.* **53** 1004
- [22] Xu L, Sadeghi N, Donnelly V M and Economou D J 2007 *J. Appl. Phys.* **101** 013304
- [23] Derouard J and Sadeghi N 1984 *J. Chem. Phys.* **81** 3002
- [24] Bruner T A, Driver R D, Smith N and Pritchard D E 1979 *J. Chem. Phys.* **70** 4155
- [25] Barnes J A, Keil M, Kutina R E and Polanyi J C 1980 *J. Chem. Phys.* **72** 6306
- [25] Barnes J A, Keil M, Kutina R E and Polanyi J C 1980 *J. Chem. Phys.* **72** 6303
- [26] Derouard J and Sadeghi N 1984 *Chem. Phys.* **88** 171
- [27] De Pristo A E, Augustin S D, Ramaswamy R and Rabitz H 1979 *J. Chem. Phys.* **71** 850
- [28] Whitaker B J and Bréchnignac P 1983 *Chem. Phys. Lett.* **95** 407
- [29] Derouard J and Sadeghi N 1983 *Chem. Phys. Lett.* **102** 324
- [30] Press W H, Teukolsky S A, Vetterling W T and Flannery B P 1992 *Numerical Recipes in Fortran* (Cambridge: Cambridge University Press) p 651, 676
- [31] Wang Q, Donnelly V M and Economou D J 2006 *J. Appl. Phys.* **100** 023301
- [32] Wang Q 2006 *PhD Dissertation* University of Houston
- [33] Boeuf J P and Pitchford L C 2005 *J. Appl. Phys.* **97** 103307
- [34] Bird R B, Stewart W E and Lightfoot E N 2002 *Transport Phenomena* 2nd edn (New York: Wiley)
- [35] Westhoff R and Szekely J 1991 *J. Appl. Phys.* **70** 3455
- [36] Brooks A N and Hughes T J R 1982 *Comput. Meth. Appl. Mech. Eng.* **32** 199